Published Online First: November, 2024
https://doi.org/10.21123/bsj.2024.10361
P-ISSN: 2078-8665 - E-ISSN: 2411-7986
Baghdad Science Journal

Preparation of novel adsorbents via functionalized MCM-41 prepared from plant residues

Raghad Saad Hatem* , ***Hayder Hamied Mihsen*** , ***Alaa Frak Hussain***

Department of Chemistry, College of Science, University of Kerbala, Kerbala, Iraq.
*Corresponding Author.

Received 03/12/2023, Revised 01/03/2024, Accepted 03/03/2024, Published Online First 20/11/2024

Abstract

In this study, mesoporous silica MCM-41 was functionalized with 3-aminopropyltriethoxysilane (APTES) to obtain MCM-41@APTES, which contains primary amine groups. In the next step, 5-bromosalicylaldehyde was refluxed with MCM-41@APTES in toluene to obtain the Schiff base-functionalized mesoporous silica material, MCM-41@APTES-BSAL. MCM-41@APTES and MCM-41@APTES-BSAL were characterized via FT-IR, FESEM-EDX, TEM, N2-adsorption-desorption, XRD, and TGA/DTA. The XRD and TEM investigations showed that MCM-41@APTES and MCM-41@APTES-BSAL were generated with extremely ordered hexagonal arrangements. The findings from the N2-adsorption–desorption analysis revealed that the average pore diameters, total pore volumes, and specific surface areas were 7.530 nm, 0.292 cm3 g−1, and 155.19 m2 g−1, and 12.654 nm, 0.055 cm3g−1, and 17.491 m2 g−1, respectively, according to the BET plots. Thermogravimetric analysis (TGA/DTA) of silica materials represented by both MCM-41@APTES and MCM-41@APTES-BSAL revealed three mass reduction steps, with the initial step involving elimination of water adsorbed via physical/chemical processes on the silica surface, a second that could be assigned to the decomposition of the organic moieties of MCM-41@APTES and MCM-41@APTES-BSAL, and a third which involved breakdown of Si-OH groups in the silica structure and their transformation into siloxane groups (Si-O-Si). The MCM-41@APTES and MCM-41@APTES-BSAL were utilized for the adsorption of heavy pollutants like cobalt and cupper ions from aqueous solution. Adsorption parameters for such uptake were determined through studying the concentration of cobalt (II) and copper (II) ions, pH, exposure time, and mass of the MCM-41@APTES and MCM-41@APTES-BSAL.

Keywords: Aqueous solution, Mesoporous material, MCM-41, Surface area, Uptake capacity.

Introduction

The unique properties of silica (SiO_2), such as its insulating abilities, its ability to act as a filler composite, and its thixotropic nature, make it an important material in use in various technological applications[1]. Silica is of particular importance in industries like glass, cosmetics, pharmaceutics, cement, and purging[2, 3]. Moreover, silica is used to utilize different organic and inorganic materials that can be used in optical applications, catalysis, and electronic coatings[4]. Mesoporous silica is used in a variety of applications, for instance, as an adsorbent surface[5], in filters and molecular sieves[6], as a method of separation[7], and participating as a catalyst in chemical reactions and the process of drug delivery[8–11]. Technologies that use silica have been increasing in number significantly, and new families of such have recently been discovered. MCM-41 is one of the forms of mesoporous silica that have attracted

Published Online First: November, 2024
https://doi.org/10.21123/bsj.2024.10361
P-ISSN: 2078-8665 - E-ISSN: 2411-7986
Baghdad Science Journal

significant interest in different fields, such as host materials for inclusion compounds and separation media catalysis[12]. Mesoporous materials contain only silanes on their surfaces as functional groups, leading to certain limitations in the use of these compounds. To overcome these limitations, various studies have been conducted in the attempt to change the active site of mesoporous silicas. The quality of these materials can be enhanced by the addition of organic groups, nanoparticles, and coordination compounds, thereby enabling the use of these materials in different ways, such as in separation methods, sensors[13–15], and catalytic processes[16, 17].

Water can be contaminated by various types of pollutants, such as radioactive isotopes, natural pollutants and, particularly, inorganic fertilizers[18]. Heavy metal ions are another significant source of pollution with regard to their effect on human health, which include species of mercury, chromium, copper, cobalt, and lead, which are all frequently present in drinking water sources. Due to their strong biological toxicities and bioaccumulation, these ions represent a serious problem in terms of the environment. Urbanization and industrialization have also increased the amount of heavy metal ions found in water supplies. Therefore, it is essential to carefully manage heavy metal ions in drinking water resources to protect the natural environment[19, 20]. Their many distinctive characteristics make ordered mesoporous silica (OMS) important to water treatment processes, which include their chemical inertness, cost-effective production, expansive pore size, abundant collection of utilitarian surface functional groups that can be tailored for exceptional selectivity towards specific pollutants, high specific surface areas, and good thermal stability[21]. The process of adsorption with porous compounds can involve different mechanisms which include hydrophobic interactions, electrostatic interactions, ion-dipole interactions, coordination by surface metal cations, ion exchange, hydrogen bonding, and dispersion forces, amongst others[22].

In this work, mesoporous materials (MCM-41@APTES and MCM-41@APTES-BSAL) derived from rice husk ash, as low-cost adsorbents, were prepared and applied in the adsorption of cobalt (II) and copper (II) metal ions from aqueous solution. Exposure time, concentration, pH, and dosage mass of adsorbent were studied as potential factors affecting the uptake of the ions.

Materials and Methods

Rice husks were collected from nearby rice production manufactures in AL-Najaf Governorate, Abbacy city. The materials used included cetyltrimethylammonium bromide (Merck, 95%), cobalt chloride hexahydrate (Merck, 98%), copper chloride dihydrate (Fluka), 99.8%), hydrochloric acid (Thomas Baker, Analar), toluene (Qrec, 99.5%), sodium hydroxide (Merck, 99%), ammonia (Qrec, 69%), acetic acid (BDH, 99.5%), nitric acid (BDH, 65%), absolute ethanol (Fluka>99%), acetone (Romal, 9.7%), (3-aminopropyl)triethoxysilane (Merck, 95%), and 5-bromosalicylaldehyde (Merck, 95%).

Instrumental

Infrared spectroscopy (8400s Shimadzu Japan, spectral range from 4000 to 400 cm^{-1}), N_2 adsorption-desorption analysis(Belsorp adsorption/desorption data analysis software BEL Japan, Inc.), powder X-ray diffraction ((Philips PW 1730/10) X-ray diffractometer using Cu Kα radiation), and scanning electron microscopy (SEM)-(FESEM MIRA III (TESCAN)/(Czech Republic)), transmission electron microscope (TEM)- EM 208S, PHILIPS, NEDERLAND, atomic force microscopy (AFM)-(NT-MDT/NTEGRA(Netherlands) and thermogravimetric analyses (TA instruments SDT-Q600 simultaneous TGA / DSC (België), from 30 to 900 ^oC at a heating rate of 20 $^oC\ min^{-1}$ under nitrogen flow. Also, the researchers used UV-Vis Spectroscopy (Shimadzu double beam 1800 UV) to determined (Co(II) and Cu(II) ions from its aqueous solutions.

Preparation of Silica (RH-SiO_2) and Mesoporous Silica (MCM-41) from Rice Husks

Silica extracted from rice husks, referred to as RH-SiO_2, and sodium silicate solution were prepared using the procedures described in reference[23]. Surfactant solutions were prepared by mixing 2.0 g of CTAB (cetyltrimethylammonium bromide) with 25 mL of deionized water. Sodium silicate was added dropwise under vigorous stirring at room temperature. Silica surfactant solution was prepared through adjusting the solution to pH 10 using acetic acid, after which the solutions were stirred at ambient temperature for six hours, followed by ageing at 100°C for 24 hours. The final mixture was filtered and rinsed with deionized water before drying at 50°C for 24 hours. The resultant materials were subjected to a calcination process at 550 ± 3°C for

Published Online First: November, 2024
https://doi.org/10.21123/bsj.2024.10361
P-ISSN: 2078-8665 - E-ISSN: 2411-7986
Baghdad Science Journal

five hours to eliminate the surfactant[24] as illustrated in scheme. 1.

Synthesis of (3-aminopropyl)triethoxysilane-Functionalized Mesoporous Silica (MCM-41@APTES)

The desired amount of MCM-41 was dried at 110°C in an oven for three hours to remove physisorbed moisture. 1.0 mL of (3-aminopropyl)triethoxysilane was add to the dried MCM-41, followed by the addition of 30 mL toluene. The mixture was then refluxed for 24 hours with stirring, and was then filtered. Toluene and ethanol were used to wash the product, which was then dried at 70°C for 24 hours. Finally, 1.20 g of the resultant material was collected as powder and labelled as MCM-41@APTES as illustrated in scheme. 1.

Synthesis of 5-bromosalicylaldehyde-Functionalized Mesoporous Silica (MCM-41@APTES-BSAL)

A mixture of 2.0 g of 5-bromosalicylaldehyde and 1.0 g of MCM-41@APTES was mixed with 30 mL of toluene to prepare MCM-41@APTES-BSAL. The mixture was refluxed at 110°C for 24 hours. The product was filtered, rinsed with toluene and then ethanol, and left to dry at 100°C for 24 hours. The final product was collected as a powder and labelled MCM-41@APTES-BSAL. A summary of this methodology is depicted in scheme 1.

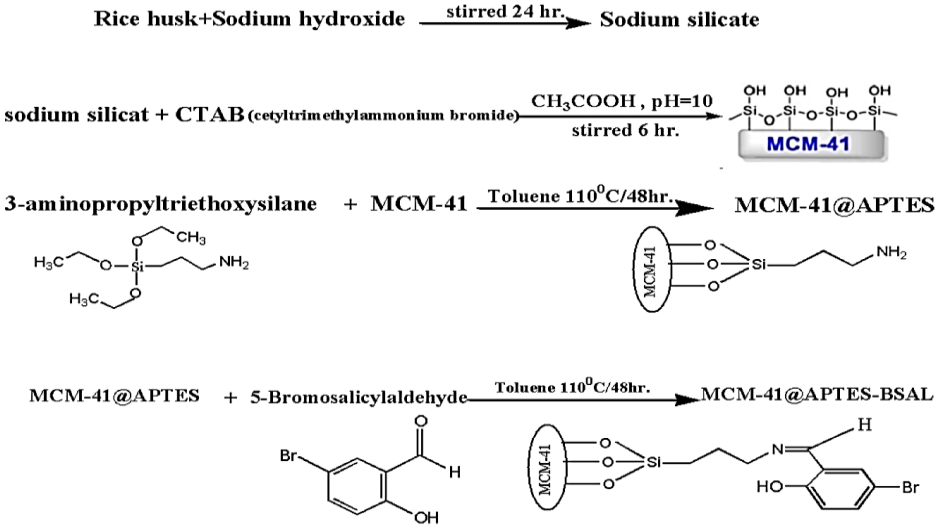

Scheme 1. The synthesis of MCM-41@APTES and MCM-41@APTES-BSAL.

Results and discussion

Characterization of the Samples Prepared

FTIR Analysis

FT-IR spectra of MCM-41@APTES and MCM-41@APTES-BSAL are illustrated in Fig. 1. The FT-IR spectra indicated the changes that occurred in MCM-41 due to functionalization with (3-aminopropyl)triethoxysilane and with 5-bromosalicylaldehyde.

The FT-IR spectrum for MCM-41, as shown in Fig. 1, exhibits several bands related to mesoporous silica. Vibrations of the hydroxyl (-O-H) group of silanol (Si-OH) give a characteristic band at approximately 3500 cm^{-1} (Si–OH)[25]. Trapped molecules of water give rise to a bending vibration at (1640 cm^{-1}) [26]. The asymmetric vibration of the siloxane group gives a broad peak at 1107 cm^{-1}, while the silanol group has an asymmetric stretching mode at (965 cm^{-1}) [27]. Additionally, stretching and bending of the siloxane group give distinct peaks at 806 and 515 cm^{-1}, respectively. In all spectra, there are three distinct peaks at around ~1000, ~800, and ~500 cm^{-1}. These peaks can be attributed to the siloxane group[28].

The FT-IR spectrum of MCM-41@APTES showed a number of absorption bands for silanol groups (Si-OH) at ~960 cm^{-1}, which was greatly reduced compared with MCM-41; this indicates successful anchoring of (3-aminopropyl)triethoxysilane. The wide peak at 3000-3200 cm^{-1} can be attributed to free NH_2. The bending vibration of N-H (primary amine) appears at 1520 cm^{-1}, while the strong peak at ~1390 cm^{-1} can be attributed to the combination of the stretching of the C-N group in primary amides. These bands show that there are propyl and amino groups on the silica. Distinct bands at 445, 935, and 1090

Published Online First: November, 2024
https://doi.org/10.21123/bsj.2024.10361
P-ISSN: 2078-8665 - E-ISSN: 2411-7986
Baghdad Science Journal

cm^{-1} can be attributed to the symmetric and antisymmetric stretching modes of Si– O–Si[28].

The FTIR spectrum of MCM-41@APTES-BSAL is illustrated in Fig. 1. The hydroxyl vibration band can be seen to have shifted to around 3400 cm^{-1}. The stretching vibration of C-H aliphatic and aromatic groups is responsible for clusters of low intensity bands at (~3000 and 2500 cm^{-1}) [26]. Schiff base ligand formation could be inferred due to the presence of the C=N group, which appeared at (1640 cm^{-1}) [29]. This provides substantial evidence that the reaction between MCM-41@APTES and 5-bromosalicylaldehyde produced C–O, whose vibrational band appears at around (1000–1300 cm^{-1}) [30].

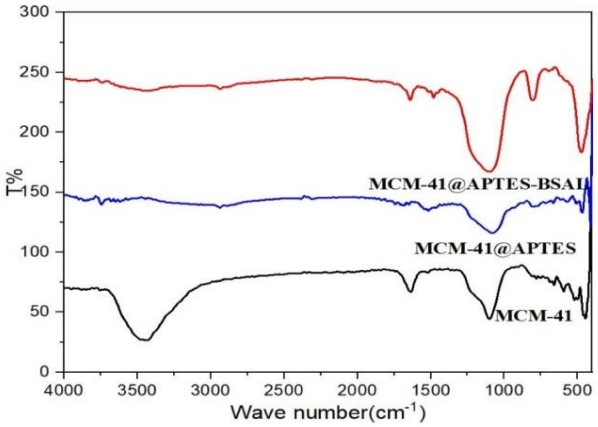

Figure 1. FTIR spectra of MCM-41@APTES and MCM-41@APTES-BSAL.

XRD Analysis

XRD analyses for data recorded at low and high angles for MCM-41@APTES and MCM-41@APTES-BSAL are presented in Figs. 2 and 3, respectively. The peak at around 2.17 (100) appeared due to the hexagonal structure of mesoporous material present in both MCM-41@APTES and MCM-41@APTES-BSAL. This was confirmed by the TEM images in Fig. 8. Filling of the honeycomb structure of the mesoporous material may lead to a lower peak intensity of MCM-41@APTES and MCM-41@APTES-BSAL compared to the MCM-41 peak [30]. The high angle XRD pattern Fig. 3 showed a broad peak at 22° due to the amorphous structures of the MCM-41@APTES and MCM-41@APTES-BSAL[31]. The crystalline size of all compounds was calculated according to the Scherrer equation[32] as shown in Table 1.

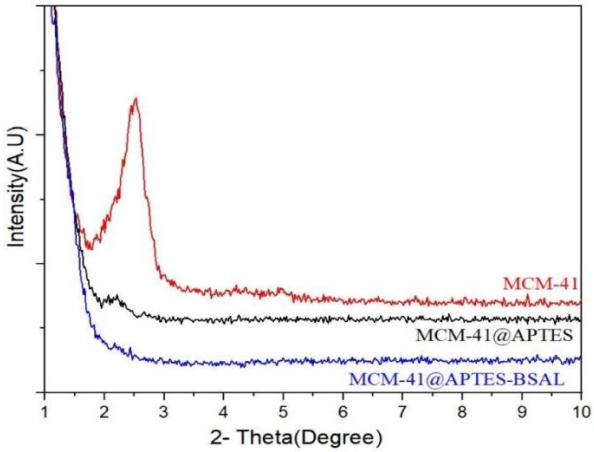

Figure 2. XRD spectra (low angle) for MCM-41, MCM-41@APTES, and MCM-41@APTES-BSAL.

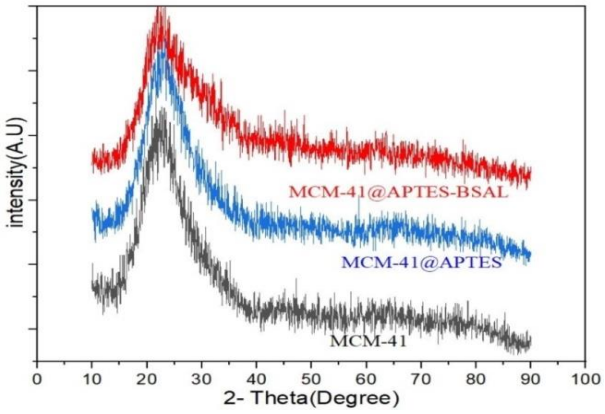

Figure 3. XRD spectra (high angle) for MCM-41, MCM-41@APTES, and MCM-41@APTES-BSAL.

Table 1. Crystallite size and Average crystallite size of MCM-41 , MCM-41@APTES and MCM-41@APTES-BSAL.

Sample	2θ = peak position (°)	β = FWHM	λ= wave length = 0.154 nm	k= Scherrer constant= 0.9	D = crystal size Average = kλ/βcos θ
MCM-41	23.10969	5.857985	0.15406	0.9	1.38
MCM-41@APTES	23.55466	1.023052	0.15406	0.9	7.93
MCM-41@APTES-BSAL	24.73328	1.26775	0.15406	0.9	6.42

N_2 Adsorption-Desorption Analysis

Specific surface area and the pore size distribution can be demonstrated via N_2 adsorption–desorption analysis. From the results presented in Figs. 4 and 5, the average pore diameters for MCM-41@APTES and MCM-41@APTES-BSAL are 7.530 nm and

Published Online First: November, 2024
https://doi.org/10.21123/bsj.2024.10361
P-ISSN: 2078-8665 - E-ISSN: 2411-7986
Baghdad Science Journal

12.654 nm, the specific surface areas are 155.19 m^2g^{-1} and 17.491 m^2g^{-1}, and total pore volumes are 0.292 cm^3 g^{-1} and 0.055 cm^3g^{-1}, respectively, according to the BET plots. The samples' porosities changed but they still had a narrow pore width distribution, which is typical for MCM-41--derivative materials[33].

The pore volumes and surface areas of MCM-41@APTES and MCM-41@APTES-BSAL decreased significantly compared to MCM-41, which has a pore volume of 126.12 cm^3 g^{-1} and a surface area of 548.92 m^2 g^{-1}. This suggests that the hexagonal pores at the surface are being blocked by large ligand molecules[30].

Hysteresis loops were detected in both MCM-41@APTES and MCM-41@APTES-BSALwithin the range 0.4 < P/Po < 1, associated with capillary condensation as per the IUPAC classification. For mesoporous solids[28], type IV is the dominant isotherm with an H_3 hysteresis loop. All samples exhibited type IV isotherms with H_3 hysteresis loops, which is characteristic of mesoporous solids. Fig. 5 illustrates the pore size distributions of MCM-41@APTES and MCM-41@APTES-BSAL. The pore ranges were observed to lie between 2 and 10 nm, which again is in the mesoporous range.

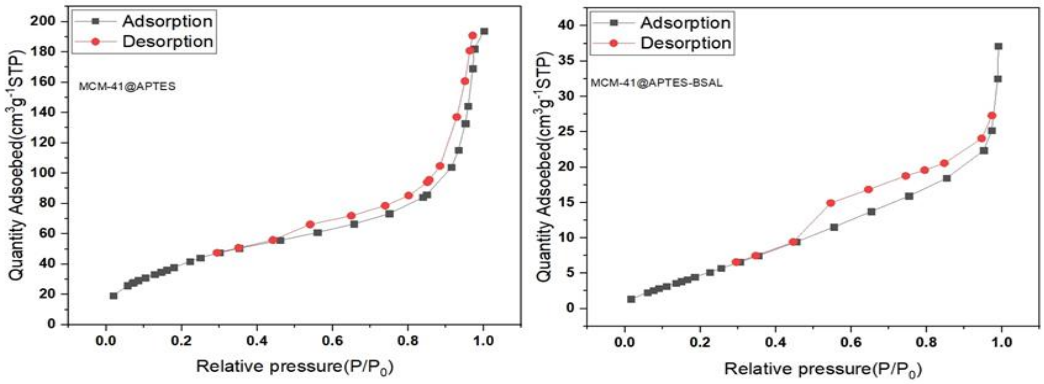

Figure 4. N_2 adsorption–desorption isotherms of MCM-41@APTES and MCM-41@APTES-BSAL materials.

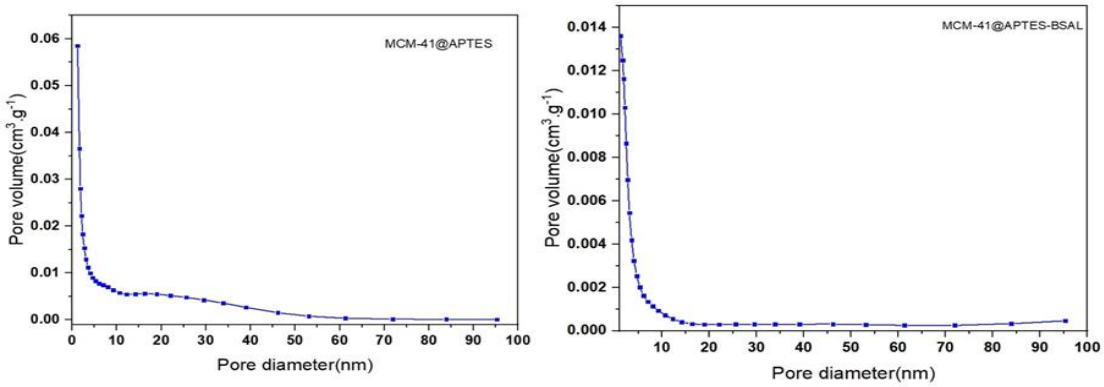

Figure 5. Pore size distributions of MCM-41@APTES and MCM-41@APTES-BSAL.

SEM and EDX Analysis

SEM images of MCM-41@APTES and MCM-41@APTES-BSAL are shown in Fig. 6. From these images, it can be seen that the particles are smooth with spherical agglomerations. The average diameters of between 20-100 nm correspond to the average diameters of mesoporous(2-5)nm and macroporous(>50nm) materials[34]. According to the EDX analysis, the presence of silicon and oxygen, in addition to nitrogen, in the solid ligand (MCM-41@APTES) was demonstrated, as can be seen in Fig. 7, from which it can be further concluded that the MCM-41 was incorporated on the (3-aminopropyl)triethoxysilane.

The EDX imaging of MCM-41@APTES-BSAL shown in Fig. 7 indicates that the compounds contained carbon, nitrogen, and bromine, in addition to oxygen and silicon elements in the complex as in Table 2. From this, it can be further concluded that the 5-bromosalicylaldehyde was incorporated onto the MCM-41@APTES.

Published Online First: November, 2024
https://doi.org/10.21123/bsj.2024.10361
P-ISSN: 2078-8665 - E-ISSN: 2411-7986
Baghdad Science Journal

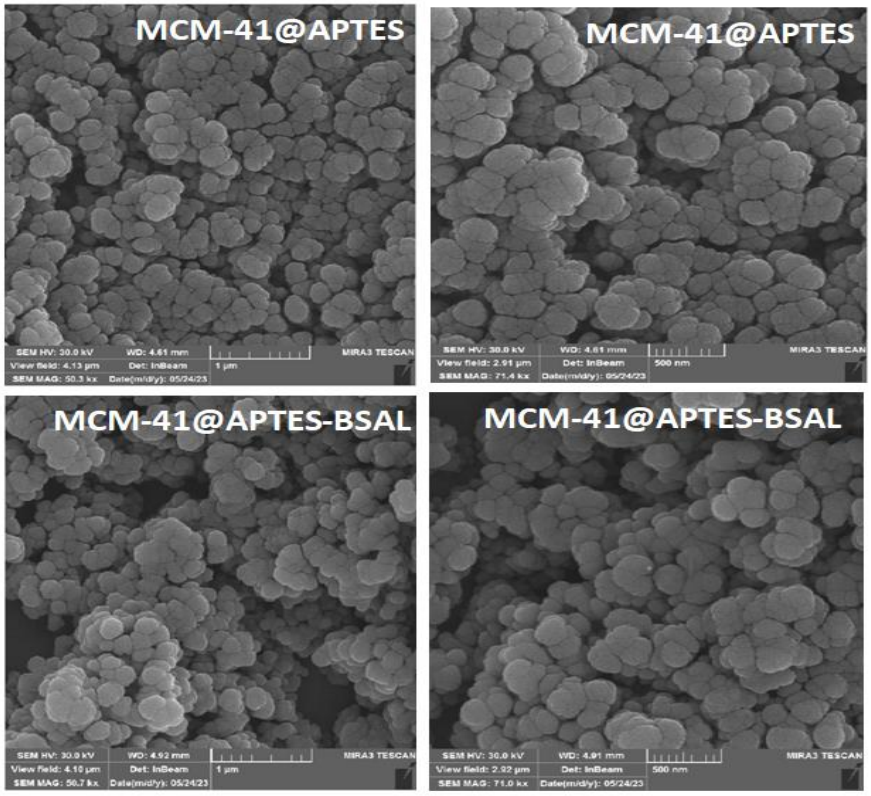

Figure 6. SEM analyses of MCM-41@APTES and MCM-41@APTES-BSAL at scales of 1000 nm and 500 nm

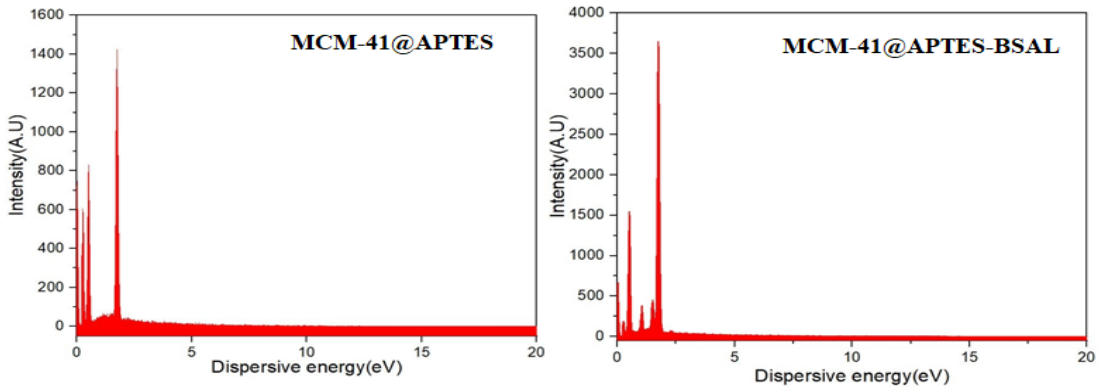

Figure 7. EDX analysis for MCM-41@APTES and MCM-41@APTES-BSAL.

Table 2. The average values obtained from EDX analysis for MCM-41@APTES and MCM-41@APTES-BSAL.

Matrials	Si Avarage mass (%)	O Avarage mass (%)	C Avarage mass (%)	N Avarage mass (%)	Br Avarage mass (%)
MCM-41@APTES	42.09	39.27	10.63	8.00	------
MCM-41@APTES-BSAL	50.43	21.88	16.72	7.32	3.65

TEM Microscopy

TEM analysis was conducted to acquire further information regarding the structural characteristics of MCM-41@APTES and MCM-41@APTES-BSAL. The associated TEM images demonstrated these species' hexagonal honeycomb structures, as shown in Fig. 8 [30, 35]. This honeycomb structure was clearly not preserved after functionalization of MCM-41 with (3-aminopropyl)triethoxysilane or with 5-bromosaliyaldehyde, because immobilization

Published Online First: November, 2024
https://doi.org/10.21123/bsj.2024.10361
P-ISSN: 2078-8665 - E-ISSN: 2411-7986
Baghdad Science Journal

of large organic compounds on the MCM-41 caused the surface to become inundated with the ligand network, blocking the pores. All species exhibited ordered porous structures consistent with previous work on MCM-41[36].

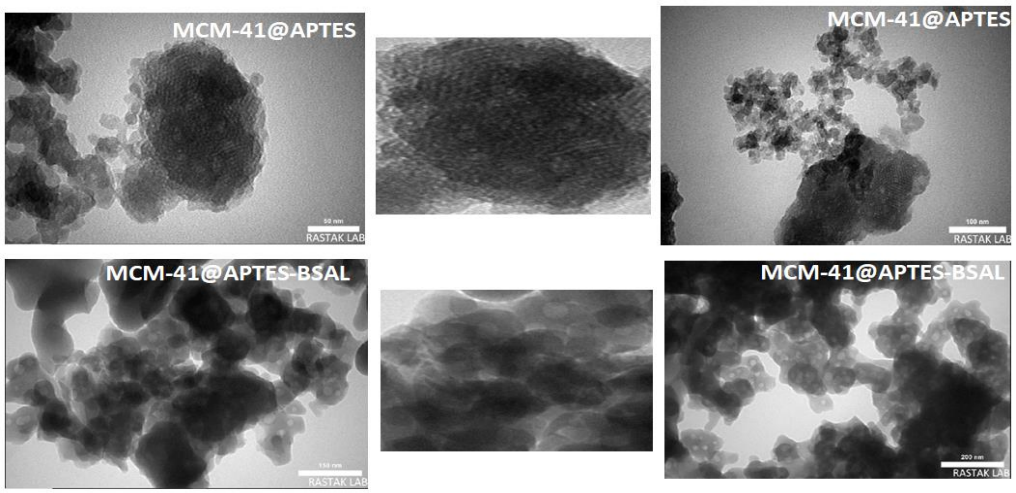

Figure 8. TEM images for MCM-41@APTES and MCM-41@APTES-BSAL at different scales.

AFM Analysis

The surface topographies of MCM-41@APTES and MCM-41@APTES-BSAL have been determined through the AFM analyses shown in Fig. 9. It was found that two-dimensional images of MCM-41@APTES's and MCM-41@APTES-BSAL's topographies were unclear, while the three-dimensional image showed the high and low topography responsible for the surface roughness of the silica surface[27]. The parameters obtained from AFM for the surface of the prepared compounds, MCM-41@APTES and MCM-41@APTES-BSAL, are illustrated in Table 3, which indicate that the roughness factor is high for MCM-41@APTES but decreased upon functionalization from 1.161 nm to 429.4 pm. This may be attributed to the successful modification of the surface of the ligand from MCM-41@APTES to MCM-41@APTES-BSAL, while the roughness factor for MCM-41@APTES-BSAL was low, indicating the relatively smooth topography that was demonstrated in SEM, TEM, and AFM analyses.

Table 3. AFM parameters for MCM-41@APTES and MCM-41@APTES-BSAL.

Sample	Average roughness (Ra)	Root square roughness (Rrms)	Average height (SZ)
MCM-41@APTES	1.161 nm	1.585 nm	12.09 nm
MCM-41@APTES-BSAL	429.4 pm	760.8 pm	9.201 nm

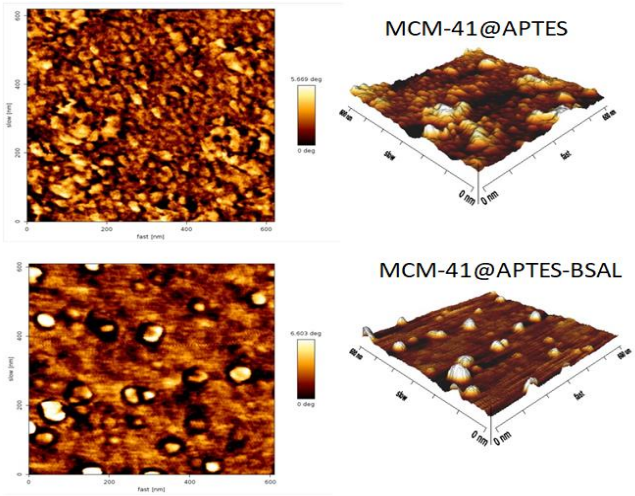

Figure 9. AFM: two-dimensional (left) and three-dimensional (right) micrographs of MC41@APTES and MCM-41@APTES-BSAL.

Published Online First: November, 2024
https://doi.org/10.21123/bsj.2024.10361
P-ISSN: 2078-8665 - E-ISSN: 2411-7986
Baghdad Science Journal

Thermal Analysis

The thermal stabilities of MCM-41@APTES and MCM-41@APTES-BSAL were investigated through TGA analysis, as illustrated in Fig. 10. The TGA results exhibited a three-stage mass production at approximately 15-900°C. The initial step involved elimination of physically/chemically adsorbed water on the silica surface, whilst the second mass loss could be assigned to the decomposition of the organic moiety in MCM-41@APTES-BSAL and MCM-41@APTES. The third step involved the breakdown of Si-OH groups in the silica structure and their transformation into Si-O-Si siloxane groups[37, 38]. The TGA spectrum showed that the compound has good thermal stability due to the fact that the percentage of loss by weight of the material is low at high temperatures[39].

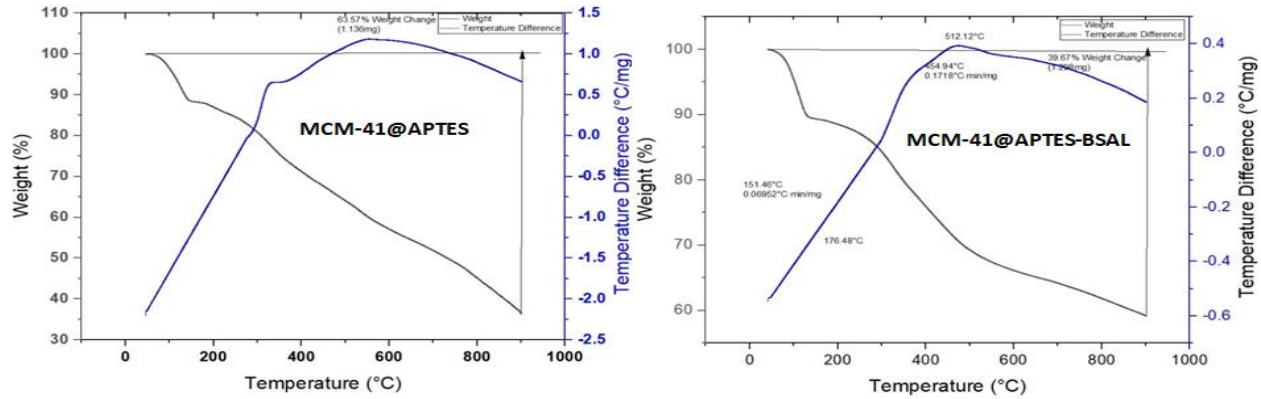

Figure 10. TGA-DTA plots of MCM-41@APTES (left) and MCM-41@APTES-BSAL (right)

Adsorption Studies

Metal Uptake Experiments

An amount of each prepared ligand, MCM-41@APTES and MCM-41@APTES-BSAL, was individually shaken with 50 mL of each metal ion, Co(II) and Cu(II). The amount of metal ion remaining was determined through enabling the insoluble complex to settle and removing a specific amount of the supernatant using a micropipette. Calibration curves for each of these ions were then constructed. The impact of different variables on the metal ions, such as time of exposure, pH, concentration of metal ions, and effect of mass of the MCM-41@APTES and MCM-41@APTES-BSAL were investigated.

Effect of Exposure Time

The uptake capacities of 0.05 M Co(II) and 0.05 M Cu(II) ions were determined by shaking the MCM-41@APTES or MCM-41@APTES-BSALwith appropriate aqueous metal solutions at various times, as illustrated in Fig. 11. It was demonstrated that there is a nonlinear increase in the uptake of metal ions as a function of the exposure time due to the diffusion factors. This increase can be initially characterized as fast ion uptake followed by a period of constant uptake as a result of blocking the pores, thus inhibiting further contact between metal ion and unreacted amine group. This hypothesis is in line with the observations of other research groups[40].

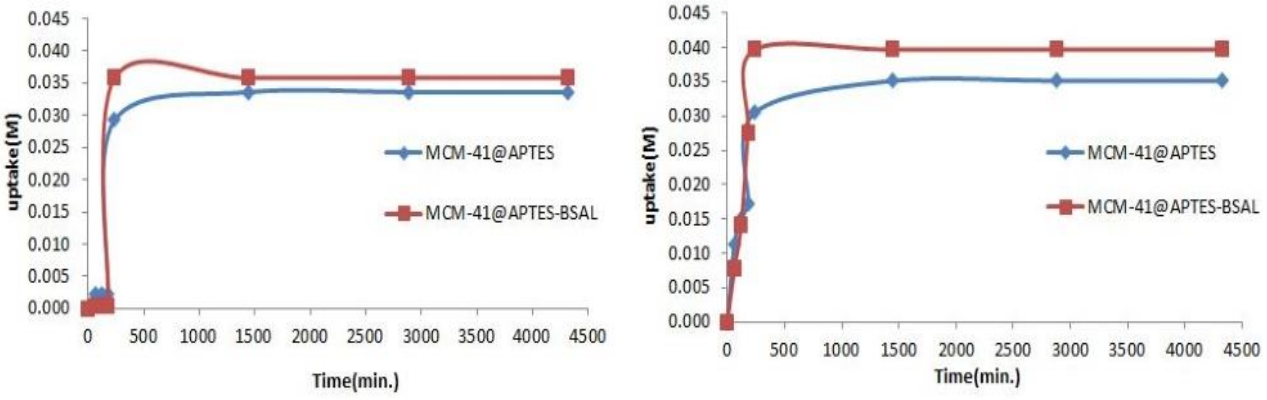

Figure 11. The uptake of Co(II) and Cu(II) ions by MCM-41@APTES and MCM-41@APTES-BSAL ligand systems versus time.

Published Online First: November, 2024
https://doi.org/10.21123/bsj.2024.10361
P-ISSN: 2078-8665 - E-ISSN: 2411-7986
Baghdad Science Journal

Effect of pH

Solutions of Co(II) (0.05 M) and Cu(II) (0.05 M) ions at various acidic pHs, adjusted via the use of NH_4OH (0.1 M)/HCL (0.1 M), were mixed with MCM-41@APTES and MCM-41@APTES-BSAL. It was observed that there was an initial increase in the uptake of metals with increasing pH. The greatest uptake of Co(II) and Cu(II) ion occurred at pH 6, as shown in Figs. 12 and 13, respectively. The pH influenced the adsorption onto the surface. The hydroxide and hydrogen ions compete to adsorb on the surface. A change in the acidity of the solution can affect the adsorption process negatively or positively[41]. When the pH is lower, more hydrogen will be gained that accumulates on the surfaces of MCM-41@APTES and MCM-41@APTES-BSAL, leading to strong competition between the released proton and metal ions for the active site on the surface, resulting in more free metal ions remaining in solution[42]. With regard to the peak value, there is no subsequent change in the amount of uptake due to the production of metal oxide[43]. The uptake of the divalent metal ions increases in the order Cu(II) > Co(II). The order of metal uptake capacities agreed with the stability constant established by Irving William and the acid base concept developed by Pearson[44].

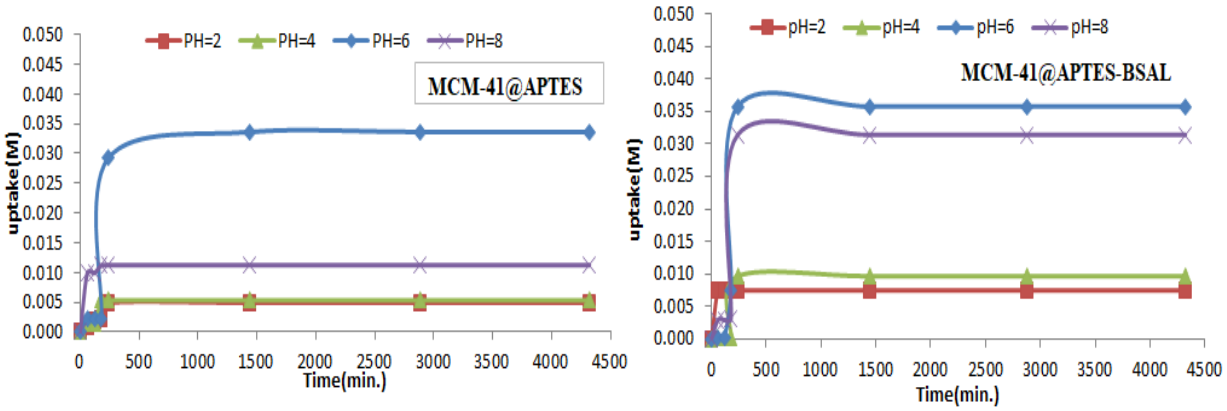

Figure 12. The uptake of Co(II) ion by MCM-41@APTES and MCM-41@APTES-BSAL at various pHs.

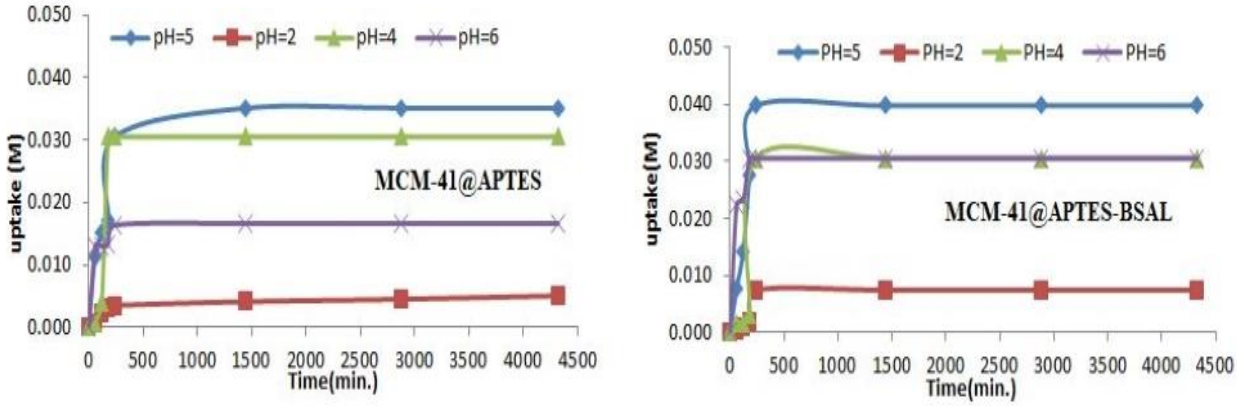

Figure 13. The uptake of Cu(II) ions by MCM-41@APTES and MCM-41@APTES-BSAL at various pHs.

Effect of Concentration of Co(II) and Cu(II) Ions

Different concentrations of cobalt and copper ions, ranging from 0.02– 0.10 M, were used to investigate the uptake capacity at optimum pH. The results given in Figs. 14 and 15 demonstrate that uptake increases with increasing concentration of Co(II) and Cu(II) ions at various times. This can be explained on the basis that each of the ions forms a 1:1 complex with the ligand at high concentration, while at low concentration there is minimal amount of uptake due to the formation of 1:2 complexes[45]; accordingly, better uptake efficiency is obtained due to the high concentration of metal ions which occupy a larger number of binding sites[46].

Published Online First: November, 2024
https://doi.org/10.21123/bsj.2024.10361
P-ISSN: 2078-8665 - E-ISSN: 2411-7986
Baghdad Science Journal

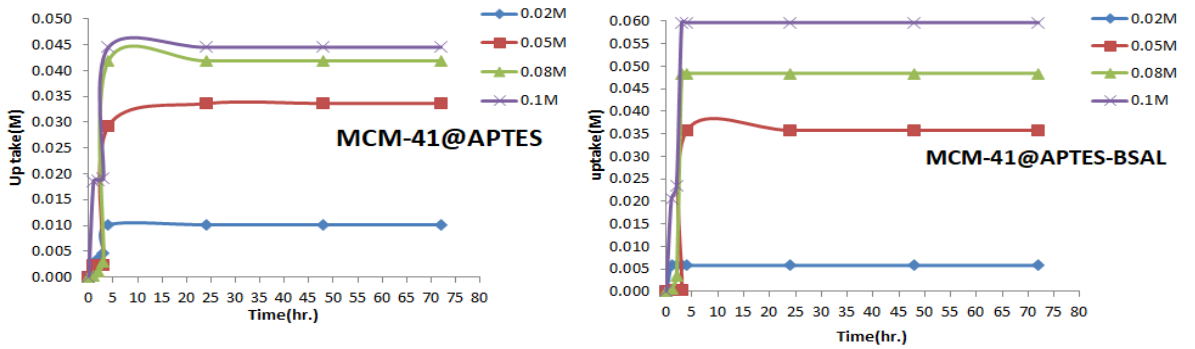

Figure 14. The uptake of Co(II) ions by MCM-41@APTES and MCM-41@APTES-BSAL at various initial concentrations.

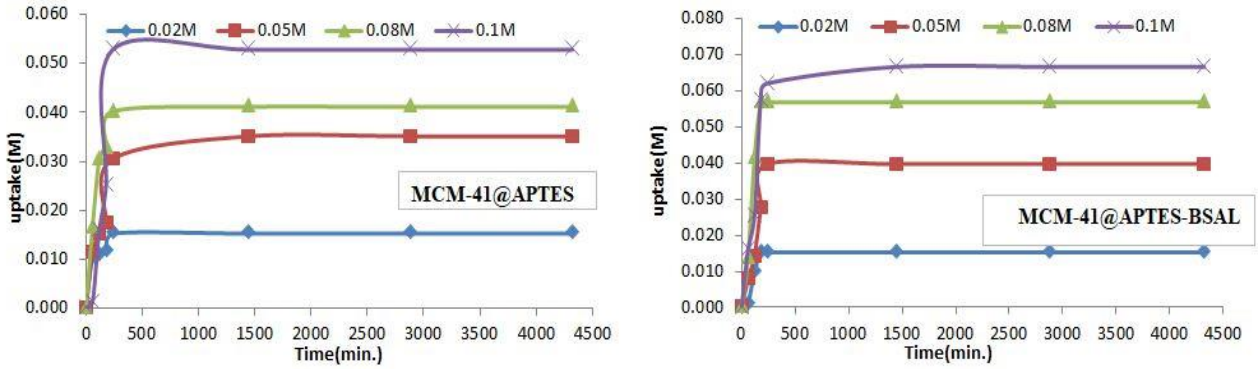

Figure 15. The uptake of Cu(II) ions by MCM-41@APTES and MCM-41@APTES-BSAL at various initial concentrations.

Effect of Mass of the MCM-41@APTES and MCM-41@APTES-BSAL

The effect of the mass of MCM-41@APTES and MCM-41@APTES-BSAL was determined by taking different amounts of absorbent (0.10, 0.15, and 0.20 g per 50 mL) in the test solutions at optimized pH for both cobalt (0.05 M) and copper (0.05 M) ions. Figs. 16 and 17 show that the uptake of Co(II) and Cu(II) ions varied as adsorbent doses were increased from 0.10 to 0.20 g. The maximum uptake of Co(II) and Cu(II) ions was found for 0.2 g MCM-41@APTES; similarly, the maximum uptake of Co(II) and Cu(II) was also found for 0.2 g MCM-41@APTES-BSAL. These findings demonstrate that there is a progressive increase in the uptake of metal ions as the adsorbent quantity was increased. However, a subsequent increase in adsorbent will not affect the uptake of Co(II) ions from the solution. This may be due to the blocking of donor sites of the solid ligand by the same ligand. The results also indicated that MCM-41@APTES-BSAL showed more efficient uptake of Co(II) and Cu(II) ions in solution than MCM-41@APTES.

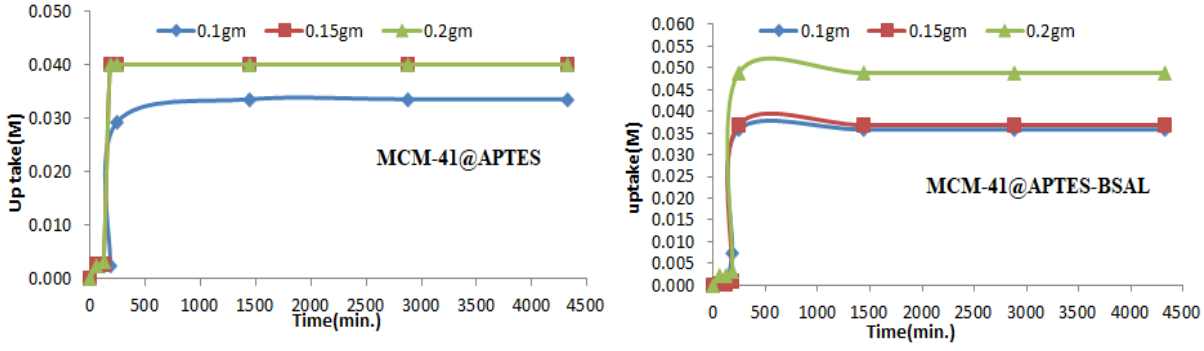

Figure 16. The uptake of Co(II) ions by MCM-41@APTES and MCM-41@APTES-BSAL with various masses.

Published Online First: November, 2024
https://doi.org/10.21123/bsj.2024.10361
P-ISSN: 2078-8665 - E-ISSN: 2411-7986
Baghdad Science Journal

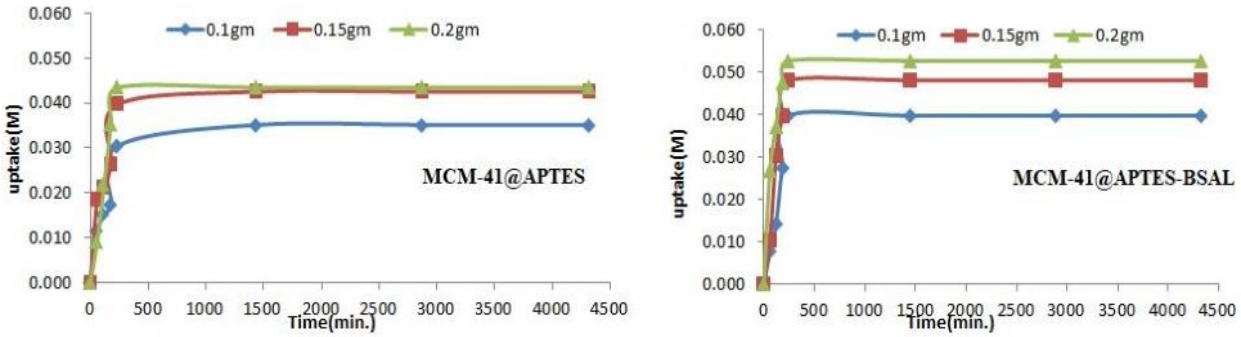

Figure 17. The uptake of the Cu(II) ion by MCM-41@APTES and MCM-41@APTES-BSAL with various masses.

Conclusion

In this research, two types of mesoporous silica (MCM-41@APTES and MCM-41@APTES-BSAL) were prepared, using silica extracted from rice husk, via functionalization of MCM-41. These species were characterized via FT-IR, XRD, and N_2 adsorption-desorption, FESEM, EDX, TEM, and TGA/DTA analyses.

The findings indicated that MCM-41@APTES and MCM-41@APTES-BSAL were synthesized with highly ordered hexagonal arrangements. BET analysis was performed to determine specific surface areas, average pore diameters, and total pore volumes. XRD diffraction analysis revealed that MCM-41@APTES and MCM-41@APTES-BSAL were amorphous in nature. Thermogravimetric analysis suggested that MCM-41@APTES and MCM-41@APTES-BSAL have the potential to remain stable, but will decompose within the temperature range of 15-900°C. The solid materials demonstrated a high efficacy in terms of uptake and extraction of copper and cobalt ions from aqueous solution. MCM-41@APTES and MCM-41@APTES-BSAL can be used in different applications, such as adsorbents for heavy metals. It was found that the uptake of ions by MCM-41@APTES-BSAL was greater than that of MCM-41@APTES.

Acknowledgment

The authors of the current research paper would like to thank Kerbala University, College of Science, and Department of Chemistry for financial support.

Author's Declaration

- Conflicts of Interest: None.
- We hereby confirm that all the Figures and Tables in the manuscript are ours. Furthermore, any Figures and images, that are not ours, have been included with the necessary permission for re-publication, which is attached to the manuscript.
- No animal studies are present in the manuscript.
- No human studies are present in the manuscript.
- No potentially identified images or data are present in the manuscript.
- Ethical Clearance: The project was approved by the local ethical committee at University of Kerbala.

Author's Contribution

R. S. H.: performed the entire experiment in its chemical parts and wrote the manuscript.

A. F. H.: supervisor of this study, and who also explained the extraction Co(II) and Cu(II) ions from aqueous solution via MCM-41@APTES and MCM-41@APTES-BSAL.

H. H. M.: Co-supervisor of the study, proposed the idea of preparing chemical compounds of silica,

interpreted the physical diagnosis, and wrote the manuscript.

References

1. Srivastava A, Singh SK. Utilization of alternative sand for preparation of sustainable mortar: A review. J Clean Prod. 2020; 253: 119706. https://doi.org/10.1016/j.jclepro.2019.119706
2. Rajeswari A, Jackcina Stobel Christy E, Gopi S, Jayaraj K, Pius A. Characterization studies of polymer-based composites related to functionalized filler-matrix interface. Interfaces in Particle and Fibre-Reinforced Composites. Elsevier; 2020. 219–250. https://doi.org/10.1016/B978-0-08-102665-6.00009-1.
3. Mirmohamadsadeghi S, Karimi K. Recovery of silica from rice straw and husk. Current Developments in Biotechnology and Bioengineering: Resource Recovery from Wastes. 2020. 411–433. https://doi.org/10.1016/B978-0-444-64321-6.00021-5.
4. Le NH, Hajjar-Garreau S, Bonne M, Megías-Sayago C, Louis B, Lebeau B, et al. Photo-induced generation of size controlled Au nanoparticles on pure siliceous ordered mesoporous silica for catalytic applications. Microporous Mesoporous Mater. 2020; 295: 109952. https://doi.org/10.1016/j.micromeso.2019.109952.
5. Ghorbani F, Kamari S. Core–shell magnetic nanocomposite of Fe_3O_4@SiO_2@NH_2 as an efficient and highly recyclable adsorbent of methyl red dye from aqueous environments. Environ Technol Innov. 2019; 14: 100333. https://doi.org/10.1016/j.eti.2019.100333.
6. Kamari S, Shahbazi A. Biocompatible Fe_3O_4@SiO_2-NH_2 nanocomposite as a green nanofiller embedded in PES–nanofiltration membrane matrix for salts, heavy metal ion and dye removal: Long–term operation and reusability tests. Chemosphere. 2020; 125282 https://doi.org/10.1016/j.chemosphere.2019.125282.
7. Bao W, Ding L, Liu Z, Zhu G, Kheshti M, Wu Q, et al. Analytically derived fixed termination time for stepwise inertial control of wind turbines—Part I: Analytical derivation. Int J Electr Power Energy Syst. 2020; 121: 106120. https://doi.org/10.1016/j.ijepes.2020.106120.
8. Sachit MA, Kareem SH. Isotherms and Thermodynamic Parameters of Metoprolol Drug Adsorption on the Prepared Mesoporous Silica. Online. Baghdad Sci J. 2023; 21 (3): 1029-1036. https://doi.org/10.21123/bsj.2023.8827.
9. Yu X, Liu S, Lin G, Yang Y, Zhang S, Zhao H, et al. KOH-activated hydrochar with engineered porosity as sustainable adsorbent for volatile organic compounds. Colloids Surfaces A Physicochem. Eng Asp. 2020; 588: 124372. https://doi.org/10.1016/j.colsurfa.2019.124372.
10. Alkafajy AM, Albayati TM. High performance of magnetic mesoporous modification for loading and release of meloxicam in drug delivery implementation. Mater. Today Commun. 2020; 23: 100890. https://doi.org/10.1016/j.mtcomm.2019.100890.
11. Dleam EA, Kareem SH. Mesoporous Silica Nanoparticles as a System for Ciprofloxacin Drug Delivery; Kinetic of Adsorption and Releasing. Baghdad Sci J. 2021; 18(2): 0357. https://doi.org/10.21123/bsj.2021.18.2.0357.
12. Costa JAS, Vedovello P, Paranhos CM. Use of Ionic Liquid as Template for Hydrothermal Synthesis of the MCM-41 Mesoporous Material. Silicon. 2020; 12(2): 289–294. https://doi.org/10.1007/s12633-019-00121-9.
13. Martínez-Carmona M, Ho QP, Morand J, García A, Ortega E, Erthal LCS, et al. Amino-Functionalized Mesoporous Silica Nanoparticle-Encapsulated Octahedral Organoruthenium Complex as an Efficient Platform for Combatting Cancer. Inorg. Chem. 2020; 59(14): 10275–10284. https://doi.org/10.1021/acs.inorgchem.0c01436.
14. Barczak M, Dobrowolski R, Borowski P, Giannakoudakis DA. Pyridine-, thiol- and amine-functionalized mesoporous silicas for adsorptive removal of pharmaceuticals. Microporous Mesoporous Mater. 2020; 299: 110132. https://doi.org/10.1016/j.micromeso.2020.110132
15. Abbas SK, Hassan ZM, Mihsen HH, Eesa MT, Attol DH. Uptake of Nickel(II) Ion by Silica-o-Phenylenediamine Derived from Rice Husk Ash. Silicon. 2020; 12(5): 1103–1110. https://doi.org/10.1007/s12633-019-00207-4.
16. Verma P, Kuwahara Y, Mori K, Raja R, Yamashita H. Functionalized mesoporous SBA-15 silica: recent trends and catalytic applications. Nanoscale. 2020; 12(21): 11333–11363. https://doi.org/10.1039/D0NR00732C.
17. Nie W, Luo Y, Yang Q, Feng G, Yao Q, Lu ZH. An amine-functionalized mesoporous silica-supported PdIr catalyst: boosting room-temperature hydrogen generation from formic acid. Inorg Chem Front. 2020; 7(3): 709–717. https://doi.org/10.1039/C9QI01375J.
18. Turan NG, Mesci B. Adsorption of copper (II) and zinc (II) ions by various agricultural by-products. Experimental studies and modelling. Environ Prot Eng. 2011; 37(4): 143- 161.
19. Chu Z, Fan X, Wang W, Huang W chiao. Quantitative evaluation of heavy metals' pollution hazards and estimation of heavy metals' environmental costs in leachate during food waste composting. Waste Manag. 2019; 84: 119–128.

Published Online First: November, 2024
https://doi.org/10.21123/bsj.2024.10361
P-ISSN: 2078-8665 - E-ISSN: 2411-7986
Baghdad Science Journal

https://doi.org/10.1016/j.wasman.2018.11.031.
20. Badamasi H, Olusola JA, Durodola SS, Akeremale OK, Ore OT, Bayode AA. Contamination Levels, Source Apportionments, and Health Risks Evaluation of Heavy Metals from the Surface Water of the Riruwai Mining Area, North-Western Nigeria. Pollution. 2023; 9(3): 929–949. https://doi.org/10.22059/poll.2023.352517.1721.
21. Diagboya PN, Olu-Owolabi BI, Adebowale KO. Microscale scavenging of pentachlorophenol in water using amine and tripolyphosphate-grafted SBA-15 silica: Batch and modeling studies. J Environ Manage. 2014; 146: 42–49. https://doi.org/10.1016/j.jenvman.2014.04.038.
22. Wu H, Xiao Y, Guo Y, Miao S, Chen Q, Chen Z. Functionalization of SBA-15 mesoporous materials with 2-acetylthiophene for adsorption of Cr(III) ions. Microporous Mesoporous Mater. 2020; 292: 109754. https://doi.org/10.1016/j.micromeso.2019.109754.
23. Ali HH, Mihsen HH, Hussain KA. Synthesis, Characterization and Antimicrobial Studies of Modified Silica Materials Derived from Rice Husks. Bionanoscience. 2023; 13(3): 1163–1176. https://doi.org/10.1007/s12668-023-01144-8.
24. Sutra P, Brunel D. Preparation of MCM-41 type silica-bound manganese(III) Schiff-base complexes. Chem Commun. 1996; (21): 2485-2486. https://doi.org/10.1039/cc9960002485.
25. Niculescu VC, Raboaca M. Efficient Rice-Husk-Derived Silica Nanocatalysts for Organic Dye Removal from Water. Catalyst. 2021; 11(7): 815. https://doi.org/10.3390/catal11070815.
26. Adam F, Batagarawa MS. Tetramethylguanidine–silica nanoparticles as an efficient and reusable catalyst for the synthesis of cyclic propylene carbonate from carbon dioxide and propylene oxide. Appl Catal A Gen. 2013; 454: 164–171. https://doi.org/10.1016/j.apcata.2012.12.009.
27. Antony R, David Manickam ST, Kollu P, Chandrasekar P V., Karuppasamy K, Balakumar S. Highly dispersed Cu(+2), Co(+2) and Ni(+2) catalysts covalently immobilized on imine-modified silica for cyclohexane oxidation with hydrogen peroxide. RSC Adv. 2014; 4(47): 24820–24830. https://doi.org/10.1039/C4RA01960A.
28. Mohamed AS, AbuKhadra MR, Abdallah EA, El-Sherbeeny AM, Mahmoud RK. The photocatalytic performance of silica fume based Co3O4/MCM-41 green nanocomposite for instantaneous degradation of Omethoate pesticide under visible light. J Photochem Photobiol A Chem. 2020; 392: 112434. https://doi.org/10.1016/j.jphotochem.2020.112434.
29. Pervaiz M, Ahmad I, Yousaf M, Kirn S, Munawar A, Saeed Z, et al. Synthesis, spectral and antimicrobial studies of amino acid derivative Schiff base metal (Co, Mn, Cu, and Cd) complexes. Spectrochim. Acta Part A Mol Biomol Spectrosc. 2019; 206: 642–649. https://doi.org/10.1016/j.saa.2018.05.057.
30. Abbas SH, Adam F, Muniandy L. Green synthesis of MCM-41 from rice husk and its functionalization with nickel(II) salen complex for the rapid catalytic oxidation of benzyl alcohol. Microporous Mesoporous Mater. 2020; 305pages?. https://doi.org/10.1016/j.micromeso.2020.110192.
31. Heydari M, Tabatabaie T, Amiri F, Hashemi SE. BTEXS Removal From Aqueous Phase by MCM-41 Green Synthesis Using Rice Husk Silica. Iran J Energy Environ. 2023; 14(4): 321–335. https://doi.org/10.5829/ijee.2023.14.04.02.
32. Fatimah S, Ragadhita R, Husaeni DF Al, Nandiyanto ABD. How to Calculate Crystallite Size from X-Ray Diffraction (XRD) using Scherrer Method. Asean J Sci Eng. 2021; 2(1): 65–76. https://doi.org/10.17509/ajse.v2i1.37647. https://doi.org/10.17509/ajse.v2i1.37647.
33. Muniandy L, Adam F, Rahman NRA, Ng EP. Highly selective synthesis of cyclic carbonates via solvent free cycloaddition of CO 2 and epoxides using ionic liquid grafted on rice husk derived MCM-41. Inorg Chem Commun. 2019; 104: 1–7. https://doi.org/10.1016/j.inoche.2019.03.012.
34. Lee CK, Chiang AST, Tsay CS. The Characterization of Porous Solids from Gas Adsorption Measurements. Key Eng Mater. 1995; 115: 21–44. https://doi.org/10.4028/www.scientific.net/KEM.115.21.
35. Kamari S, Ghorbani F. Extraction of highly pure silica from rice husk as an agricultural by-product and its application in the production of magnetic mesoporous silica MCM–41. Biomass Convers Biorefinery. 2021; 11: 3001–3009. https://doi.org/10.1007/s13399-020-00637-w.
36. Appaturi JN, Adam F. A facile and efficient synthesis of styrene carbonate via cycloaddition of CO2 to styrene oxide over ordered mesoporous MCM-41-Imi/Br catalyst. Appl Catal B Environ. 2013; 136–137: 150–159. https://doi.org/10.1016/j.apcatb.2013.01.049.
37. Rout L, Mohan A, Thomas AM, Ha CS. Rational design of thermoresponsive functionalized MCM-41 and their decoration with bimetallic Ag–Pd nanoparticles for catalytic application. Microporous Mesoporous Mater. 2020; 291: 109711. https://doi.org/10.1016/j.micromeso.2019.109711.
38. Vaysipour S, Rafiee Z, Nasr-Esfahani M. Synthesis and characterization of copper (II)-poly(acrylic acid)/M-MCM-41 nanocomposite as a novel mesoporous solid acid catalyst for the one-pot synthesis of polyhydroquinoline derivatives. Polyhedron. 2020; 176:114294. https://doi.org/10.1016/j.poly.2019.114294.
39. Cheng SZD, Li CY, Calhoun BH, Zhu L, Zhou WW. Thermal analysis: the next two decades. Thermochim Acta. 2000; 355(1–2): 59–68. https://doi.org/10.1016/S0040-6031(00)00437-8.
40. Yang JJ, El-Nahhal IM, Chuang IS, Maciel GE. Synthesis and solid-state NMR structural characterization of polysiloxane-immobilized amine

Published Online First: November, 2024
https://doi.org/10.21123/bsj.2024.10361
P-ISSN: 2078-8665 - E-ISSN: 2411-7986
Baghdad Science Journal

ligands and their metal complexes. J.Non-Cryst Solids. 1997; 209: 19–39. https://doi.org/10.1016/S0022-3093(96)00534-0.
41. Ouyang D, Zhuo Y, Hu L, Zeng Q, Hu Y, He Z. Research on the Adsorption Behavior of Heavy Metal Ions by Porous Material Prepared with Silicate Tailings. Minerals 2019; 9(5): 291. https://doi.org/10.3390/min9050291.
42. Witek-Krowiak A, Szafran RG, Modelski S. Biosorption of heavy metals from aqueous solutions onto peanut shell as a low-cost biosorbent. Desalination. 2011. 126–134. https://doi.org/10.1016/j.desal.2010.07.042.
43. El-Nahhal IM, Zaggout FR, El-Ashgar NM. Uptake of divalent metal ions (Cu2+, Zn2+ and Cd2+) by polysiloxane immobilized monoamine ligand system. Anal Lett. 2000; 23: 2031–2053. https://doi.org/10.1080/00032710008543173.
44. El-Ashgar NM, El-Nahhal IM, Ahmed MA, Abu Shaweesh AA, Chehimi MM. Synthesis, characterization, and metal uptake of multiple functionalized immobilized-polysiloxane diamine-thiol chelating ligand derivatives. J Iran Chem Soc. 2018; 15(10): 2325–2338. https://doi.org/10.1007/s13738-018-1421-0.
45. Zaggout FR, El-Nahhal IM, El-Ashgar NM. Uptake of divalent metal ions (Cu2+, Zn2+, and Cd2+) by polysiloxane immobilized diamine ligand system. Anal Lett. 2001; 34(2): 247–266. https://doi.org/10.1081/AL-100001577.
46. Georgin J, Dotto GL, Mazutti MA, Foletto EL. Preparation of activated carbon from peanut shell by conventional pyrolysis and microwave irradiation-pyrolysis to remove organic dyes from aqueous solutions. J Environ Chem Eng. 2016; 4(1): 266–275. https://doi.org/10.1016/j.jece.2015.11.018.

تحضير مواد مازه جديده بواسطة توظيف MCM-41 المحضر من بقايا النباتات

رغد سعد حاتم ، حيدر حميد محسن ،علاء فراك حسين

قسم الكيمياء، كلية العلوم، جامعة كربلاء، كربلاء، العراق.

الخلاصة

في هذه الدراسه MCM-41 (مركبات السليكا المساميه) تم توظيفها بالتفاعل مع 3-امينوبروبيل تراي ايثوكسي سيلان (APTES) لانتاج MCM-41@APTES الذي يحتوي على مجموعة امين اوليه .في الخطوه اللاحقه 5-بروموسالسلديهايد تفاعل مع MCM-41@APTES بوجود التلوين للحصول على قاعدة شيف الموظفه من مركبات السليكا المساميه MCM-41@APTES-BSAL المركبات MCM-41@APTES وMCM-41@APTES-BSAL الجديده تم تشخيصها بااستخدام FT-IR, FESEM-EDX, TEM, N2-adsorption –desorption, XRD TGA/DTA. تحليل XRDوTEM اظهرت ان المركبات المحضره MCM-41@APTES and MCM-41@APTES-BSAL هي سداسيه الترتيب.النتائج لتقنية N_2-adsorption–desorption اشارت الى ان معدل قطر الفجوه و مجموع حجم الفجوه ومساحه السطح المخصصه هي 7.530 nmو$0.292\ cm^3\ g^{-1}$ و$155.19\ m^2\ g^{-1}$ و12.654 nm و$0.055\ cm^3 g^{-1}$ و $17.491\ m^2\ g^{-1}$ على التوالي بالاعتماد على نتائج BET. التحاليل الحرايه ل MCM-41@APTESوMCM-41@APTES-BSAL اظهرثلاث خطوات في فقدان الوزن والخطوه الاولى فقدان الماء الممتزعبر عملية فيزيائيه اوكيميائيه على سطح السليكا والخطوه الثانيه تتضمن تحليل الماده العضويه لـ MCM-41@APTES and MCM-41@APTES-BSAL .الخطوه الثالثه تتضمن كسر مجموعة Si-OH في تركيب السليكا وتحولها الى مجموعة سايلوكسان (Si-O-Si) .

MCM-41@APTESوMCM-41@APTES-BSAL استخدم لامتزاز بعض الايونات الثقيله مثل الكوبلت والنحاس من محاليلها المائيه. تم دراسة العوامل المؤثره على الامتزازمثل تركيز ايون الكوبلت والنحاس الثنائيه وتاثير الداله الحامضيه وزمن التعرض والوزن المؤثر لMCM-41@APTES and MCM-41@APTES-BSAL

الكلمات المفتاحية: محاليل مائية، مواد مسامية، MCM-41، مساحة السطح، سعة الامتزاز.